

www.acsami.org Research Article

# Elimination of Multidrug-Resistant Bacteria by Transition Metal Dichalcogenides Encapsulated by Synthetic Single-Stranded DNA

Abhishek Debnath, Sanchari Saha, Duo O. Li, Ximo S. Chu, Zachary W. Ulissi, Alexander A. Green,\* and Qing Hua Wang\*



Cite This: ACS Appl. Mater. Interfaces 2021, 13, 8082-8094



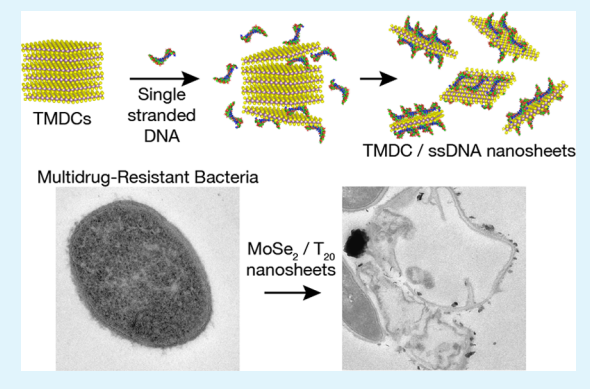
**ACCESS** I

Metrics & More

Article Recommendations

Supporting Information

ABSTRACT: Antibiotic-resistant bacteria are a significant and growing threat to human health. Recently, two-dimensional (2D) nanomaterials have shown antimicrobial activity and have the potential to be used as new approaches to treating antibiotic resistant bacteria. In this Research Article, we exfoliate transition metal dichalcogenide (TMDC) nanosheets using synthetic single-stranded DNA (ssDNA) sequences, and demonstrate the broad-spectrum antibacterial activity of  $MoSe_2$  encapsulated by the  $T_{20}$  ssDNA sequence in eliminating several multidrug-resistant (MDR) bacteria. The  $MoSe_2/T_{20}$  is able to eradicate Gram-positive Escherichia coli and Gram-positive Staphylococcus aureus at much lower concentrations than graphene-based nanomaterials. Eradication of MDR strains of methicillin-resistant S. aureus (MRSA), Enterococcus faecalis, Pseudomonas aeruginosa, Klebsiella pneumoniae, and Acinetobacter baumannii are shown to



occur at at 75  $\mu$ g mL<sup>-1</sup> concentration of MoSe<sub>2</sub>/T<sub>20</sub>, and *E. coli* at 150  $\mu$ g mL<sup>-1</sup>. Molecular dynamics simulations show that the thymine bases in the T<sub>20</sub> sequence lie flat on the MoSe<sub>2</sub> surface and can, thus, form a very good conformal coating and allow the MoSe<sub>2</sub> to act as a sharp nanoknife. Electron microscopy shows the MoSe<sub>2</sub> nanosheets cutting through the cell membranes, resulting in significant cellular damage and the formation of interior voids. Further assays show the change in membrane potential and reactive oxygen species (ROS) formation as mechanisms of antimicrobial activity of MoSe<sub>2</sub>/T<sub>20</sub>. The cellular death pathways are also examined by mRNA expression. This work shows that biocompatible TMDCs, specifically MoSe<sub>2</sub>/T<sub>20</sub>, is a potent antimicrobial agent against MDR bacteria and has potential for clinical settings.

KEYWORDS: two-dimensional materials, antimicrobial activity, antibacterial activity, transition metal dichalcogenides, DNA, multidrug-resistant bacteria, MRSA, E. coli

#### ■ INTRODUCTION

Antibiotic drug resistance is a pressing threat to global health. Spurred by the misuse and overuse of commonly prescribed antibiotics, drug-resistant bacteria are becoming increasingly common, and infections that were once easily treated can now force patients into extended hospital stays. In the United States alone, infections by drug-resistant bacteria have been estimated to cause 2 million cases of serious illness and 23 000 deaths each year, leading to billions of dollars in economic and societal costs. Despite this threat, the number of antibiotics under development remains low, raising the possibility of rampant drug resistance reversing many of the advances of modern medicine. Thus, this global health challenge demands new approaches to combatting and eradicating bacterial infections.

Nanostructured materials of various compositions and morphologies have been studied for their potential as antimicrobial agents. Two-dimensional (2D) materials have emerged as promising antibacterial materials owing to their high surface areas and atomically thin edges, which can

promote strong interactions with bacterial cell walls, and in some cases, the ability to generate redox species to trigger cell death. Among these materials, graphene and graphene oxide (GO) and their derivatives have been extensively studied and have provided varying levels of antibacterial activity depending on the preparation and treatment method. Per example, GO paper showed 98.5% Escherichia coli inhibition at 85  $\mu$ g mL<sup>-1</sup>, whereas 100% elimination was observed for Pseudomonas aeruginosa at 100  $\mu$ g mL<sup>-1</sup>. Electrochemically produced graphene quantum dots induced oxidative stress in bacteria and eliminated 80% of E. coli and 92% of Staphylococcus aureus. Transition metal dichalcogenides (TMDCs), which have been shown to have better biocompat-

Received: December 28, 2020 Accepted: February 2, 2021 Published: February 11, 2021





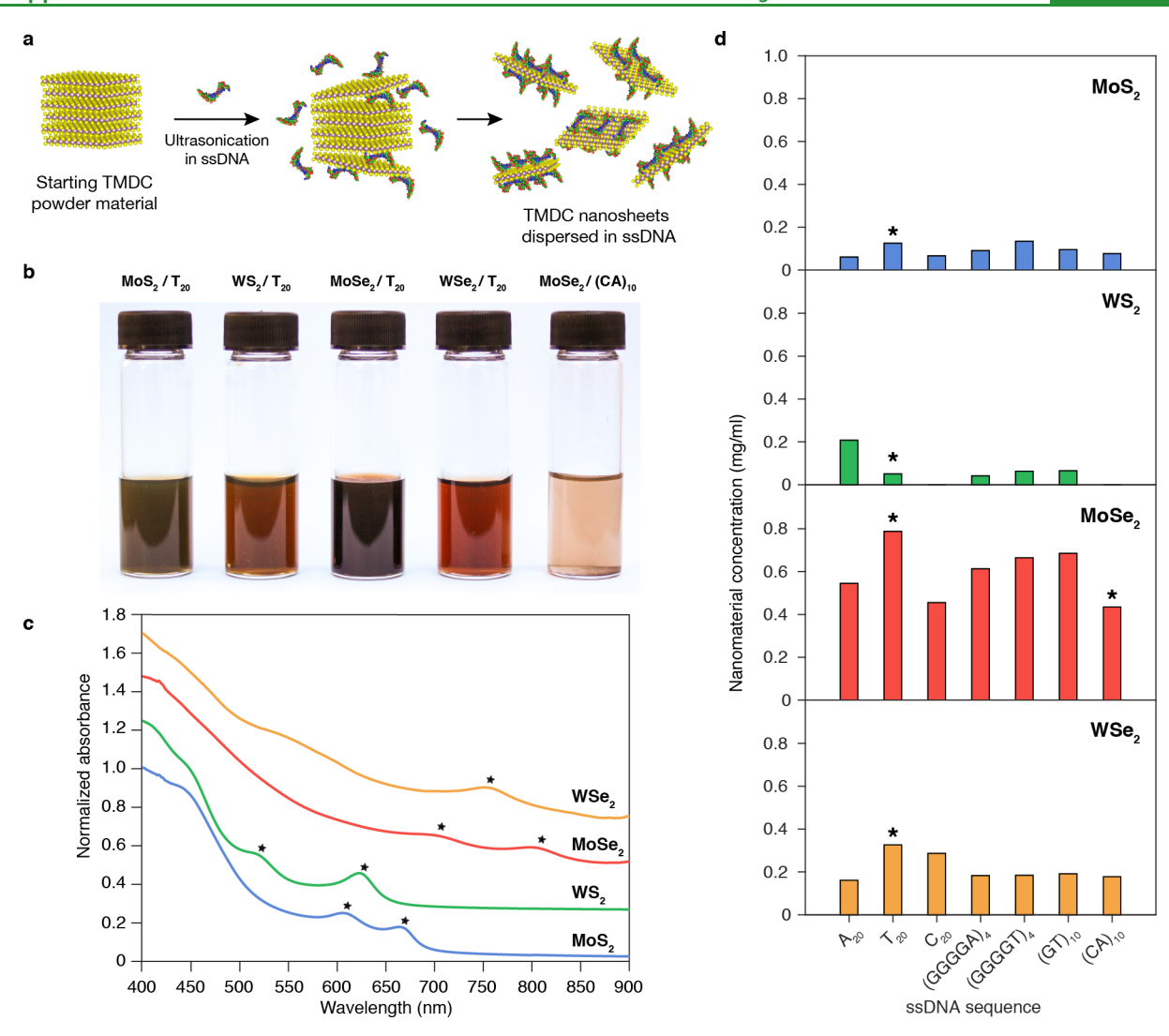
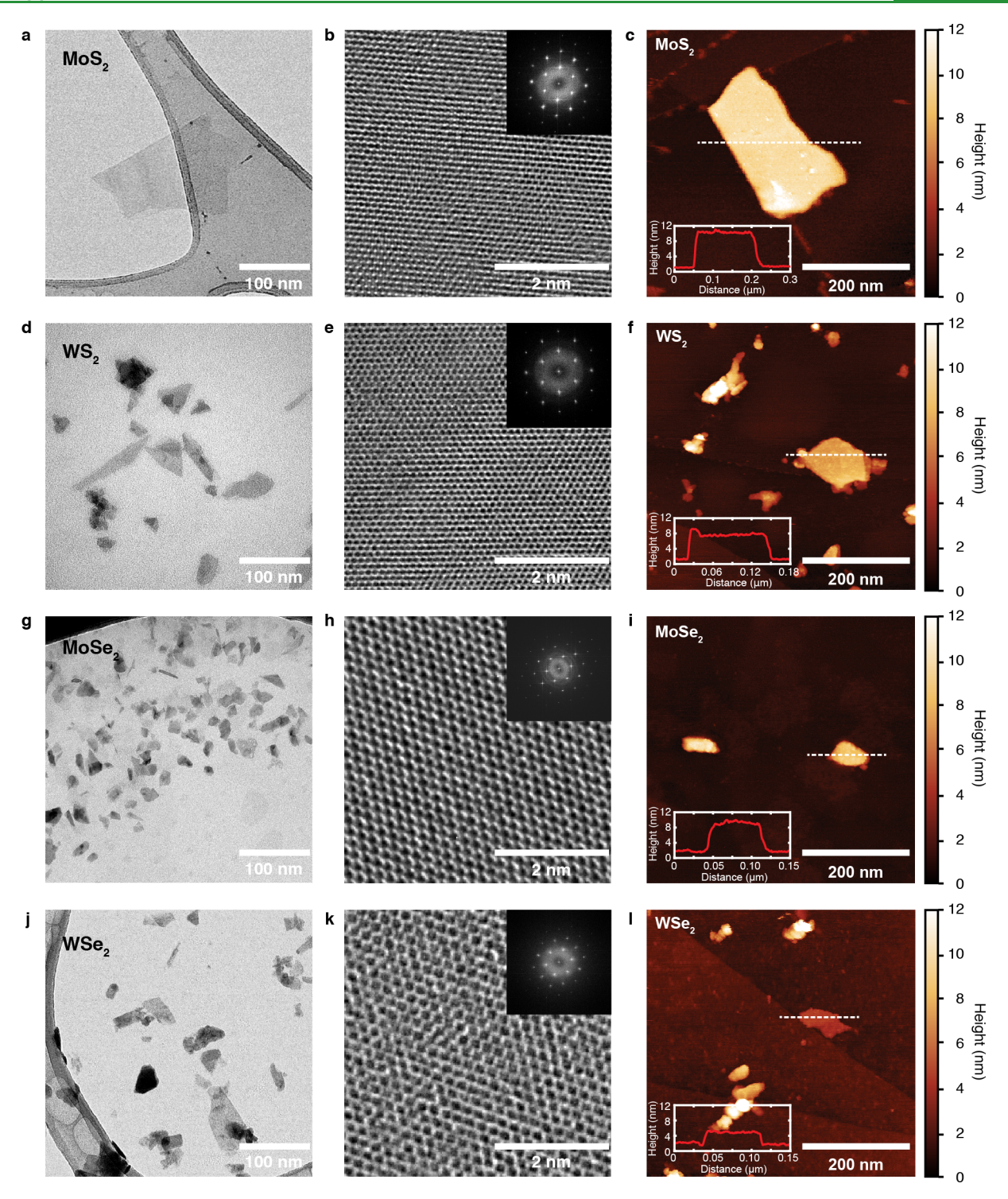


Figure 1. Dispersion of two-dimensional transition metal dichalcogenides in ssDNA. (a) Schematic illustration showing encapsulation of 2D TMDCs with short ssDNA strands. (b) Photograph of vials of the four different 2D TMDCs dispersed in the  $T_{20}$  ssDNA sequence and showing the differences in dispersion efficiency for  $MoSe_2$  by  $T_{20}$  and  $(CA)_{10}$ . (c) UV-vis absorption spectra of ssDNA dispersed TMDCs, with excitonic peaks indicated by (\*) symbols. (d) Plots of concentrations of TMDC dispersions as a function of DNA sequence. The dispersions shown in panel b are indicated by an asterisk (\*).

ibility than graphene and can be enzymatically degraded, have also been studied for antibacterial activity. 22-31 Chemically exfoliated MoS<sub>2</sub>, for example, successfully killed 93.4% of E. coli cells upon exposure at 80  $\mu$ g mL<sup>-1</sup>,<sup>27</sup> and WSe<sub>2</sub> coated by long strands of salmon-derived DNA eliminated 82.3% of the same bacteria.<sup>32</sup> Hydrothermally synthesized WS<sub>2</sub> was shown to kill 98.67% and 99.98% of E. coli and Bacillus subtilis cells, respectively, but only at very high concentrations of 250 µg mL<sup>-1</sup>.30 WS<sub>2</sub> dispersed in surfactant solutions completely eliminated cultures of E. coli and S. aureus, but it exhibited significant toxicity toward human cell lines.<sup>29</sup> A water disinfection system that employed vertically aligned MoS2 layers and visible light was able to eliminate >99.999% of E. coli and Enterococcus faecalis cells but would not be suitable for treating bacterial infections in patients.<sup>28</sup> Nanosheets of other 2D materials,<sup>5</sup> such as MXenes<sup>33–36</sup> and metal organic frameworks,<sup>37</sup> have also been studied for their antimicrobial applications.

Herein, we describe a novel preparation of 2D TMDCs that provides remarkable broad-spectrum antibacterial activity

against multidrug-resistant (MDR) strains of both Grampositive and Gram-negative bacteria. These antibacterial materials consist of 2D TMDCs coated by short sequences of single-stranded DNA (ssDNA). By using appropriate sequences of ssDNA, we successfully prepared stable dispersions of MoS2, MoSe2, WS2, and WSe2 in aqueous solution and confirmed their two-dimensional character using transmission electron microscopy (TEM) and atomic force microscopy (AFM). We chose ssDNA to disperse the TMDCs because they have previously been used to disperse carbon nanotubes, 38-45 are biocompatible, and can be used to interface with other biomolecules. We find that MoSe<sub>2</sub> nanosheets encapsulated by the T<sub>20</sub> ssDNA sequence have the highest concentration, do not exhibit toxicity against a human cell line, yet are capable of complete elimination of many MDR pathogens, which are the most common causes of bacterial infections in U.S. hospitals, at concentrations as low as 75 µg mL<sup>-1</sup> for S. aureus, E. faecalis, P. aeruginosa, Klebsiella pneumoniae, and Acinetobacter baumannii and as low as 150 µg mL<sup>-1</sup> for E. coli, and provide substantially higher antibacterial



**Figure 2.** Microscopic analysis of TMDC dispersions. Left column: TEM images demonstrating successful production of two-dimensional (a) MoS<sub>2</sub>, (d) WS<sub>2</sub>, (g) MoSe<sub>2</sub>, and (j) WSe<sub>2</sub> nanosheets. Middle column (b, e, h, k): Corresponding HRTEM images of atomic structures of nanosheets (insets show electron diffraction patterns showing crystallinity). Right column (c, f, i, l): Corresponding AFM images of nanosheets deposited from ssDNA dispersions onto HOPG substrates by spin coating. Insets: Height profiles along the dashed lines across each nanosheet.

activity than widely studied graphene oxide and other preparations of 2D TDMCs. We use molecular dynamics (MD) simulations to show that the  $T_{20}$  ssDNA sequence lies very flat on the  $MoSe_2$  surface, thus enhancing the dispersion efficiency of the nanosheets, and allows them to more effectively interact with the bacterial cells. Mechanistic studies show that the  $MoSe_2$  nanosheets cut through cell membranes, cause membrane depolarization, and reactive oxygen species

(ROS) production to trigger cell death. A detailed comparison to the antibacterial performance of other 2D materials and nanomaterials is also conducted; while some nanomaterials may have been reported with antibacterial properties at comparable or lower concentrations, our work presents other benefits, such as relatively short incubation times, broad spectrum effectiveness against a wide range of MDR bacteria, and simplicity of preparation.

## ■ RESULTS AND DISCUSSION

Exfoliation and Encapsulation of 2D TMDCs Using **Short ssDNAs.** Short synthetic ssDNA sequences were used for exfoliation and stabilization of four TMDC compounds: MoS<sub>2</sub>, MoSe<sub>2</sub>, WS<sub>2</sub>, and WSe<sub>2</sub>. On the basis of the amphiphilic structure of ssDNA, we anticipated that the hydrophobic DNA bases 46 would undergo strong  $\pi$ -stacking interactions with the hydrophobic surfaces of the TMDCs (typically with water contact angles in the ~70-90° range depending on sample preparation details), 47-50 enabling the hydrophilic sugarphosphate ssDNA backbone to interface with surrounding water molecules. The negatively charged phosphate groups in the backbone would also provide strong electrostatic repulsion to suspend each flake in solution and prevent nanosheet restacking (Figure 1a). Given the sequence dependence of ssDNA dispersions of carbon nanotubes, 51 we investigated the ability of seven 20-nucleotide (nt) ssDNAs containing different sequences of the four canonical DNA bases adenine (A), cytosine (C), guanine (G), and thymine (T) to disperse the TMDCs. These sequences contained 20-mer repeats of the bases (A20, C20, and T20) or they consisted of repeated pairs of noncomplementary bases ((GT)<sub>10</sub>, (CA)<sub>10</sub>). Since long guanine repeats are challenging to synthesize, we instead studied the guanine-rich ssDNAs (GGGGA)<sub>4</sub> and (GGGGT)<sub>4</sub>.

Bulk TMDC powders (200 mg each for MoSe<sub>2</sub> and WSe<sub>2</sub> and 100 mg each for MoS<sub>2</sub> and WS<sub>2</sub>) were probe ultrasonicated in aqueous solutions containing 0.2 mg mL<sup>-1</sup> of synthetic ssDNA. The ultrasonicated solutions were then centrifuged and the resulting supernatants were collected. Figure 1b provides a photograph of the strongly colored and stable 2D TMDCs dispersions prepared using the common sequence T<sub>20</sub>, which was an effective sequence for dispersing all four of the TMDCs. Optical absorbance spectroscopy of the dispersions confirmed successful exfoliation of the TMDCs revealing the characteristic excitonic transition peaks for the four compounds (Figure 1c). The visual appearance of the vials indicates the formation of stable dispersions, but further characterization was used to quantify the effectiveness of the dispersions. The concentrations of the TMDCs dispersed in the synthetic ssDNAs were determined using inductively coupled plasma mass spectrometry (ICP-MS) as shown in Figure 1d and are the maximum saturation concentrations for each combination. MoSe<sub>2</sub> and WSe<sub>2</sub> yielded dispersions with the highest loadings, with several ssDNA sequences producing dispersions at or above 200  $\mu g$  mL<sup>-1</sup>. The maximum concentration was observed for MoSe<sub>2</sub>/T<sub>20</sub> at a little below 800  $\mu$ g mL<sup>-1</sup>, obtained for optimal ssDNA sequences. The sulfur-containing MoS<sub>2</sub> and WS<sub>2</sub> displayed lower loadings, in general, with typical concentrations of 50  $\mu$ g mL<sup>-1</sup>.

We note that the starting quantities of the bulk powder at 100 mg (for MoS<sub>2</sub> and WS<sub>2</sub>) and 200 mg (for MoSe<sub>2</sub> and WSe<sub>2</sub>) are both in significantly in excess compared to the amount of ssDNA in the dispersing solution, with only about 1–2% of the starting mass of bulk TMDCs ending up successfully dispersed as nanosheets. However, we observed that starting with 200 mg of bulk MoS<sub>2</sub> and WS<sub>2</sub> tended to result in less effective dispersions. We believe a possible explanation is related to differences in affinities between the ssDNA and TMDCs, so that in some cases the amount of ssDNA may be effectively consumed by adsorption to the TMDC powders, rather than participating in the exfoliation and stabilization of the nanosheets. Therefore, for those

TMDCs (i.e., the selenides), the lower starting amount of bulk powder perhaps counterintuitively led to better results. Further optimization of the starting amount of bulk powders was not conducted since both amounts are far in excess of the ssDNA concentration and resulted in saturation concentrations of each nanosheet dispersion.

We evaluated the stability of the DNA-wrapped TMDCs using zeta potential measurements (Figure S1), which gives a measure of the surface charge of the nanosheets. We found MoSe<sub>2</sub> and WSe<sub>2</sub> to be the most stable with zeta potential values of -42.13 and -40.13 mV, respectively, whereas MoS<sub>2</sub> and WS<sub>2</sub> were less stable with zeta potential values of -21.13 and -20.07 mV, respectively. We observed significant variations in the concentration of dispersed TMDCs depending on the sequence of ssDNA used and the composition of the TMDC. In general, the highest concentration dispersions were obtained for the T<sub>20</sub> sequence, whereas (CA)<sub>10</sub> was the weakest out of the sequences studied. Our study also revealed thymine and guanine showed better affinity toward all TMDCs compared to cytosine and adenosine. The repeating dinucleotide sequence GT was also tested with ssDNAs of different lengths, in particular 10-nt, 20-nt, and 40-nt lengths. We found that (GT)<sub>10</sub> provided the highest concentrations among the three and that MoS<sub>2</sub> ssDNA with (GT)<sub>5</sub> was unstable and aggregated within a few hours.

The successfully exfoliated 2D TMDCs using low molecular weight ssDNA were structurally characterized using TEM and high-resolution transmission electron microscopy (HRTEM) and AFM as shown in Figure 2. TEM imaging of the exfoliated TMDCs revealed their geometries as 2D nanosheets. The average lateral size of nanoflakes decreased in order from MoS<sub>2</sub>, WS<sub>2</sub>, MoSe<sub>2</sub>, and WSe<sub>2</sub> (Figure 2a-d). MoS<sub>2</sub> yielded nanoflakes with lateral dimensions of approximately 80-100 nm, WS<sub>2</sub> and MoSe<sub>2</sub> about 60-70 nm, and WSe<sub>2</sub> less than 50 nm. AFM images of MoS<sub>2</sub> confirmed the presence of flakes with extended lateral dimensions with thicknesses of around 10 nm (Figure 2e). The WS<sub>2</sub> dispersion showed the secondlargest flakes with thicknesses below 10 nm (Figure 2f), whereas MoSe<sub>2</sub> and WSe<sub>2</sub> exhibited the smallest flakes with thicknesses around 10 nm or less (Figure 2g) and ~5 nm (Figure 2h), respectively. The measured thicknesses of TMDC flakes also include a uniform layer of ssDNA, which covers both sides of the TMDC flakes. The AFM and TEM data correlate well with each other and both showed successful ssDNA-based exfoliation of TMDCs to produce nanosheets. Overall, we obtain primarily few- and multilayer TMDC nanosheets from this LPE process with a distribution of thicknesses and areas, which is consistent with previous results in the literature for LPE-derived nanosheets. 52,53 We further studied the crystal structure of DNA-dispersed TMDCs using HRTEM (Figure 2a-d). These images show that the TMDCs retain the expected hexagonal lattice structure of pristine 2H phase of the TMDCs following encapsulation by short ssDNAs.

Molecular Dynamics Simulations for Representative ssDNA/2D TMDC Surface Structures. We performed molecular dynamics simulations to better understand the observed sequence-dependent encapsulation effects and the coating formed the ssDNA around the 2D TMDC's. Literature efforts had previously characterized the interaction energy and representative ssDNA conformations for single base pairs and short uniform sequences  $(G_6, T_6, A_6, C_6)$ . S4,55 For three of the sequences,  $(GT)_{10}$ ,  $(CA)_{10}$ , and  $T_{20}$ , and two 50 nm  $\times$  50 nm

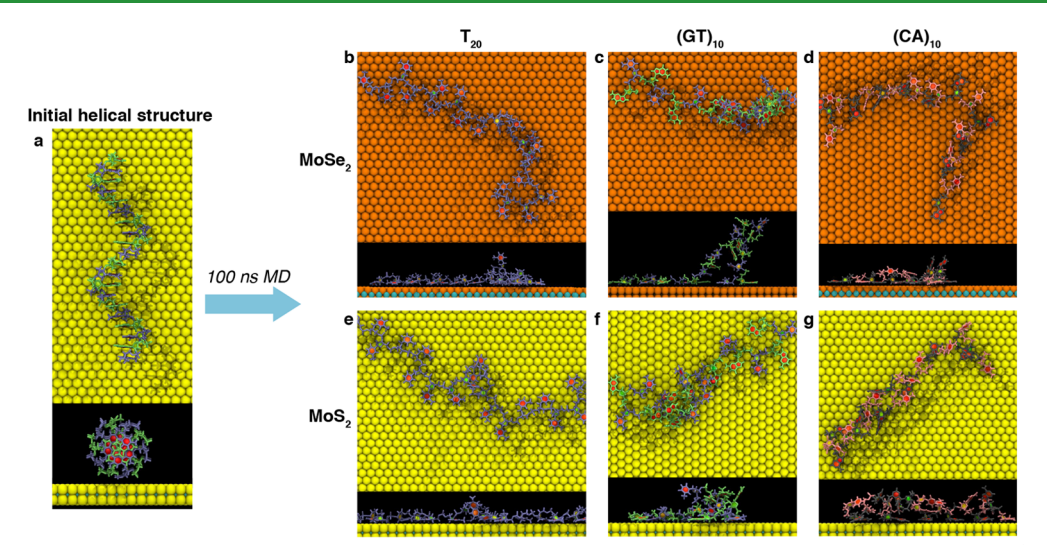


Figure 3. Molecular dynamics simulations. (a) ssDNA structures in an initial helical structure were placed onto  $MoSe_2$  and  $MoS_2$  surfaces and simulated for 100 ns. The resulting structures for  $MoSe_2$  (b, c, d) and  $MoS_2$  (e, f, g) show that there are more base pairs lying flat on the surfaces in the  $T_{20}$  sequence (b, e) than in the  $(GT)_{10}$  and  $(CA)_{10}$  sequences which have many bases in configurations that protrude from the surfaces.

2D TMDC sheets (MoS<sub>2</sub> and MoSe<sub>2</sub>), we performed long time scale molecular dynamics relaxations of approximately 100 ns per system using the NAMD software<sup>56</sup> and VMD for visualization.<sup>57</sup> The force field (CHARMM<sup>58</sup>), parameters, and explicit water model were chosen for consistency with previous studies,<sup>54</sup> with final structures shown in Figure 3. We found that the T<sub>20</sub> sequences consistently had the strongest interaction energy with the 2D TMDCs and formed extended flat sequences along the surface such that every base pair was in contact with the 2D TMDCs. The  $(GT)_{10}$  sequences for both 2D TMDCs had similar structures for base pairs adsorbed to the surface driven by T base adsorption but had extended sequences protruding from the surface that could possibly lead to thicker adsorption layers than the tightly bound T<sub>20</sub> strands. The (CA)<sub>10</sub> strands tended to form stacked structures with A bases adsorbed to the surface and C bases adsorbed on top of those. These results qualitatively explain the observed trends in dispersion concentrations shown in Figure 1. We also calculated just the interaction energy between the ssDNA and the 2D TMDC sheets (i.e., ignoring water energetics), with T<sub>20</sub> having uniformly the strongest interaction, as expected since every base pair was adsorbed. For all three sequences the interaction energy was less strong for the MoSe<sub>2</sub> surfaces than for the MoS<sub>2</sub> surfaces, suggesting that interaction energy was inversely correlated with experimental solubility. Thermodynamic free energy adsorption energy calculations could describe these interactions more accurately but the time scales associated with adsorption and desorption of such large molecules was prohibitively expensive.

**Mammalian Cell Viability of MoSe**<sub>2</sub>/ssDNA. Since the MoSe<sub>2</sub>/ $T_{20}$  dispersions had the highest concentrations, we chose to study their effect on killing bacterial cells while remaining compatible with human cells. To assess their biocompatibility, MoSe<sub>2</sub>/ $T_{20}$  nanosheets were added to cultures of the model AS49 human epithelial cell line. Concentrations of MoSe<sub>2</sub>/ $T_{20}$  ranging from 25 to 250  $\mu$ g mL<sup>-1</sup> were applied to cultures for 72 h and mammalian cell viability was determined using the colorimetric MTT assay (see Methods section for full details). No significant toxicity was observed for MoSe<sub>2</sub>/ $T_{20}$  up to a 175  $\mu$ g mL<sup>-1</sup> concentration of MoSe<sub>2</sub>, with greater than 90% cell viability

as shown in Figure S2. At concentrations above this, there was an observed decrease in cell viability. The range of concentrations with cell viability >90% completely spans the concentrations required for eradication of bacteria, as shown in the sections below, indicating excellent cell viability at the relevant antibacterial concentrations. We also verified the bacterial viability in four different growth media, as shown in Figure S3.

Antibacterial Activity of MoSe<sub>2</sub>/ssDNA. Having confirmed the viability of mammalian cells in the presence of MoSe<sub>2</sub>/T<sub>20</sub> nanosheets, we next evaluated their effect on two representative strains of Gram-negative and Gram-positive bacteria, E. coli MG1655 and Staphylococcus aureus subsp. aureus (ATCC 29213), respectively, as shown in Figure 4a-d. For determination of antibacterial activity, logarithmic-phase bacteria at a concentration of 10<sup>7</sup> cell-forming units per mL (CFU mL<sup>-1</sup>) were treated with MoSe<sub>2</sub>/T<sub>20</sub> dispersions at different concentrations for 4 h. Microdilutions of the treated bacteria were then applied to agar and incubated overnight for colony counting the next day. The MoSe<sub>2</sub>/T<sub>20</sub> dispersions displayed exceptional antibacterial activity against both species of bacteria. We observed 100% elimination of S. aureus at a concentration of 75  $\mu$ g mL<sup>-1</sup> of MoSe<sub>2</sub>/T<sub>20</sub> (Figure 4a), and of E. coli at 150  $\mu$ g mL<sup>-1</sup> (Figure 4b).

We also compared the performance of the  $MoSe_2/T_{20}$  dispersion with carbon-based 2D nanomaterials, which have recently been studied for their antibacterial activity.  $^{10,12,19,35,59}$  We chose graphene oxide (GO) and graphene dispersed in dsDNA based on their bactericidal effect from a recent report which showed GO was the most effective of the carbon-based materials,  $^{12}$  and exposed them to the same *E. coli* and *S. aureus* strains with the same procedures as described above. As shown in Figure 4a and b,  $MoSe_2/T_{20}$  was significantly more effective than both graphene and GO across many concentrations at killing these strains of bacteria as determined by colony counting. At the higher concentrations we tested,  $MoSe_2/T_{20}$  exhibited orders of magnitude higher antibacterial activity than GO and graphene.

To determine the role of the encapsulating material around the  $MoSe_2$  nanosheets for antibacterial performance, we then carried out comparative studies using  $MoSe_2$  encapsulated by

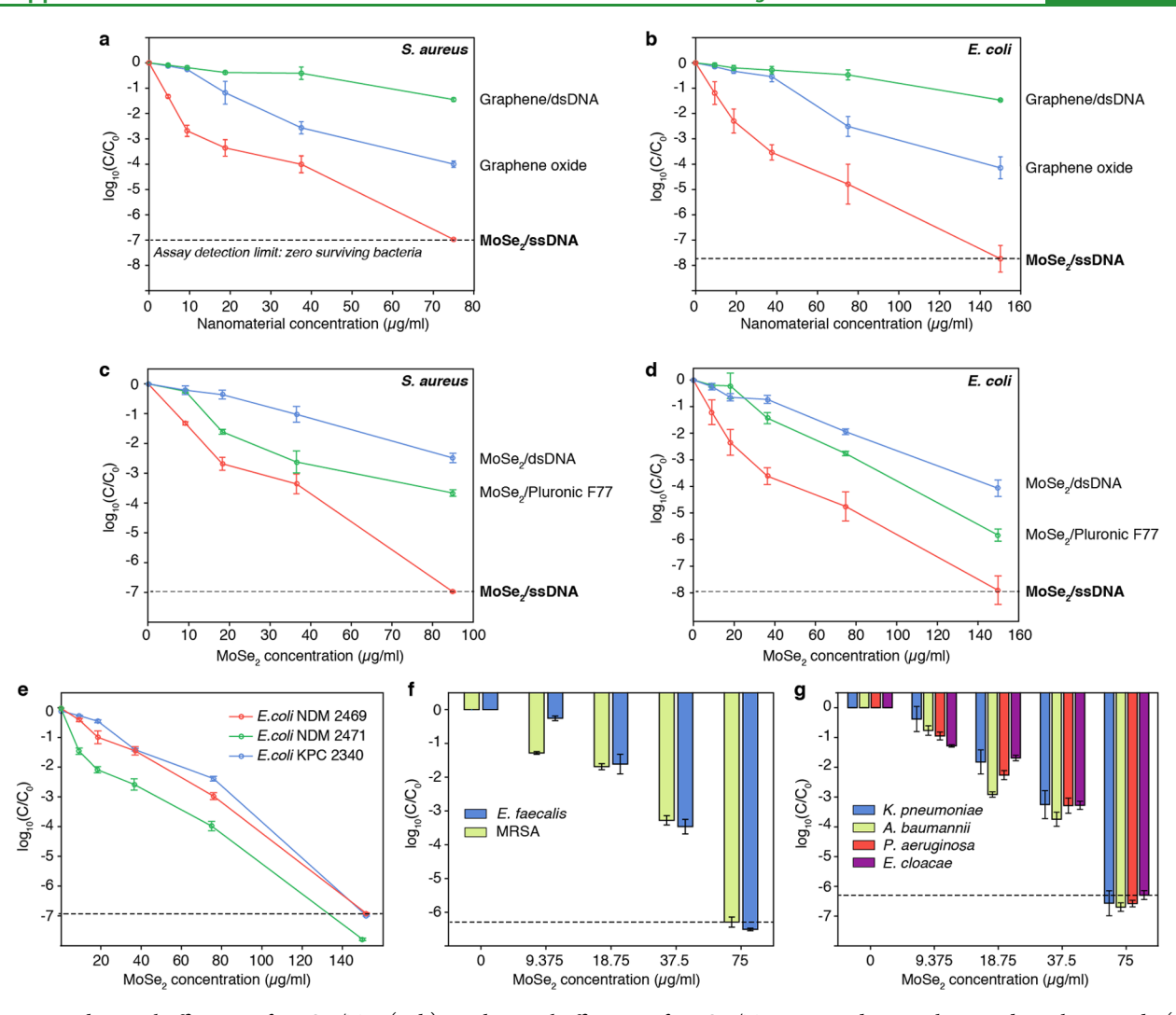


Figure 4. Antibacterial efficiency of  $MoSe_2/T_{20}$ . (a, b) Antibacterial efficiency of  $MoSe_2/T_{20}$  compared to graphene and graphene oxide (GO) using (a) model Gram-positive *S. aureus* and (b) Gram-negative *E. coli* MG1655. (c, d) Antibacterial efficiency of  $MoSe_2/T_{20}$  compared to  $MoSe_2$  dispersed with Pluronic F77 and salmon genomic dsDNA using (c) *S. aureus* and (d) *E. coli*. (e) Antibacterial activity of  $MoSe_2/T_{20}$  against three MDR *E. coli* strains. (f) Antibacterial activity of  $MoSe_2/T_{20}$  against Gram-positive *E. faecalis* and MRSA strains. (g) Antibacterial activity of  $MoSe_2/T_{20}$  against Gram-negative *K. pneumoniae*, *A. baumannii*, *P. aeruginosa*, and *E. cloacae* strains.

two additional biocompatible polymers: long genomic doublestranded DNA (dsDNA) purified from salmon testes because a recent report showed that WSe2 suspended using genomic dsDNA had 2-fold higher antibacterial activity than GO,<sup>32</sup> and the block copolymer Pluronic F77 because it has been widely used for preparing biocompatible dispersions of 2D nanosheets.<sup>60</sup> In our results shown in Figure 4c and d, we found that MoSe<sub>2</sub>/T<sub>20</sub> showed significantly stronger bactericidal properties than MoSe<sub>2</sub>/dsDNA and MoSe<sub>2</sub>/F77 against S. aureus and E. coli for nearly all the concentrations tested and provided stronger enhancements as the concentration increased.  $MoSe_2/T_{20}$  showed 4 and 3 orders of magnitude higher killing toward S. aureus compared to MoSe<sub>2</sub>/long genomic DNA and MoSe<sub>2</sub>/F77, respectively. At 150 μg mL<sup>-</sup> concentrations, MoSe<sub>2</sub>/T<sub>20</sub> completely eradicated E. coli, which corresponded to the elimination of all 10<sup>7</sup> cells treated, while the activity of MoSe<sub>2</sub>/dsDNA and MoSe<sub>2</sub>/F77 was 2.2 and 3.2 orders of magnitude weaker, respectively.

We attribute the variation in antibacterial properties with different encapsulating polymers to changes in the thickness of the polymer coating around each  $MoSe_2$  nanosheet. The

Pluronic F77 employs bulky poly(ethylene oxide) chains to suspend the MoSe<sub>2</sub> in the aqueous environment, <sup>60</sup> but they also block direct interactions between the MoSe2 and the bacterial cell wall. For the genomic dsDNA, the use of long DNA sequences also prevents the formation of a thin, conformal ssDNA coating around the MoSe<sub>2</sub>. In contrast, the short length of the T<sub>20</sub> sequence has many bases that lie flat on the WSe<sub>2</sub> surface as shown by the calculations in Figure 3, which enables the ssDNA to effectively coat and spread out along the MoSe<sub>2</sub> surface to stabilize the nanosheets in solution. The thin coating of the T<sub>20</sub> sequence results in very thin structures that can both physically pierce the bacterial cell wall and allow closer interaction of the MoSe<sub>2</sub> with the membrane for depolarization, as we show in the mechanistic studies below. Furthermore, simple thermodynamic arguments suggest that molecules with proportionally larger length and adsorption energies (same base pair sequences) will, at the same base pair concentration in solution, result in higher surface packing densities than for shorter molecules with smaller adsorption energies since the free energy of adsorption is in an exponential (for small coverages). At high coverages,

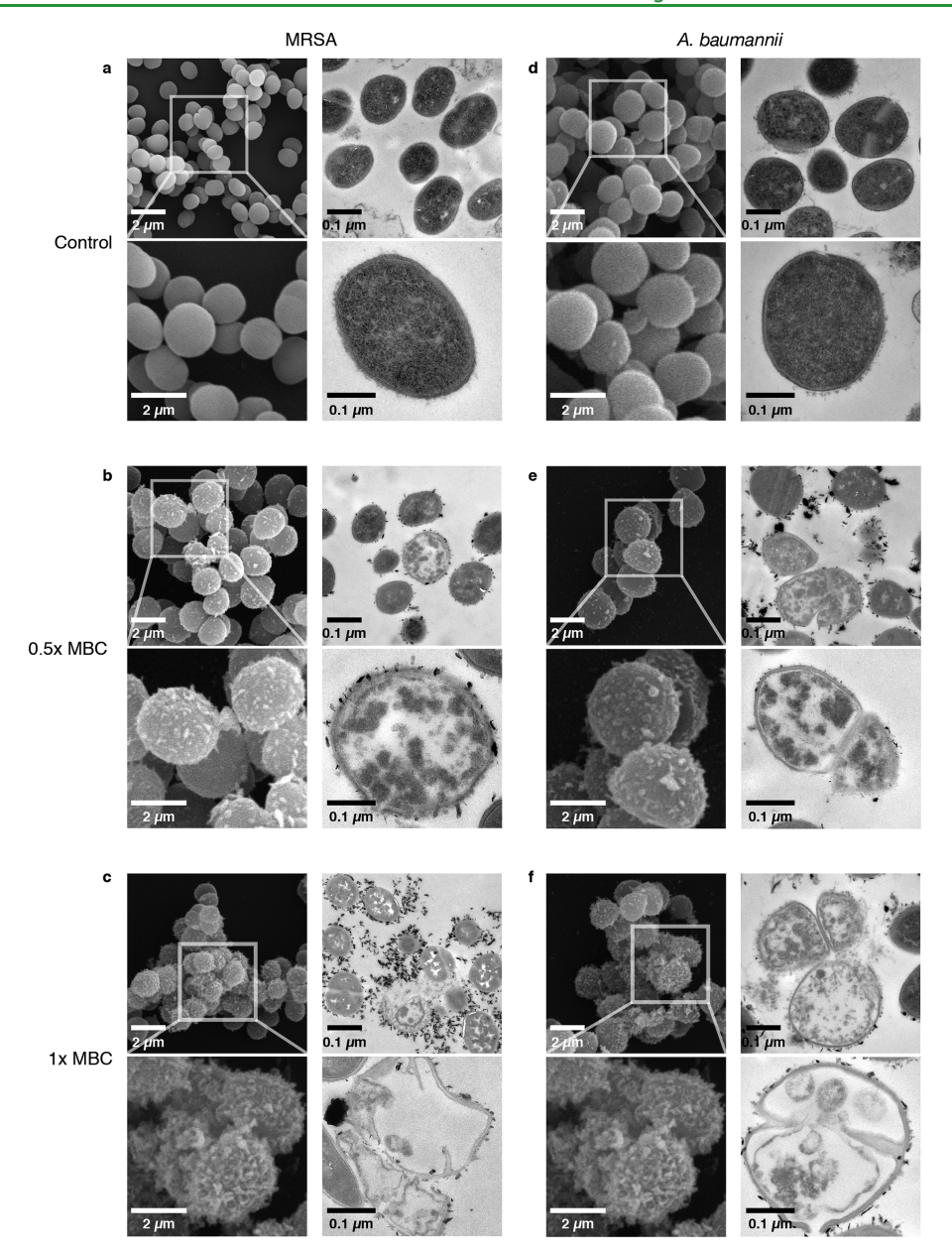


Figure 5. Morphological changes of bacteria after exposure to  $MoSe_2/ssDNA$ . Images of Gram-positive MRSA and Gram-negative *A. baumannii* from SEM (images with dark backgrounds) and TEM (images with light backgrounds) for (a, d) untreated control, (b, e)  $0.5 \times MBC$  at 37  $\mu g$  mL<sup>-1</sup> of  $MoSe_2/T_{20}$ , and (c, f)  $1 \times MBC$  at 75  $\mu g$  mL<sup>-1</sup> of  $MoSe_2/T_{20}$ .

DNA-DNA repulsion will become important and so the precise structure of the partially adsorbed chains is crucial.

Antibacterial Studies against Multidrug-Resistant Bacteria. The recent emergence of nosocomial infections by bacteria with broad-spectrum resistance to antibiotics in hospitals and clinics requires novel broad-spectrum antibacterial strategies. We sought to determine if the  $MoSe_2/T_{20}$  dispersions retained their exceptional bactericidal activity against several multidrug-resistant (MDR) strains. We first evaluated three strains of MDR *E. coli* carrying resistance to carbapenems, a class of antibiotic agents often used to combat drug-resistant infections. *E. coli* NDM 2469 and *E. coli* NDM 2471 strains both carry the New Delhi metallo- $\beta$ -lactamase (NDM), a recently identified carbapanemase, while *E. coli* KPC 2340 carries the *Klebsiella pneumoniae* carbapenemase (KPC). All three strains exhibit broad-spectrum resistance to multiple families of antibiotics. Antibiotic resistance tests

conducted by ATCC on the NDM 2469 and NDM 2471 strains indicated that these strains were resistant to 33 and 32 out of 35 antibiotics tested, respectively. Studies by ATCC on *E. coli* KPC 2340 indicated that it was resistant to 30 out of the 34 antibiotics evaluated. The three MDR *E. coli* strains were exposed to different concentrations of MoSe<sub>2</sub>/T<sub>20</sub> for 4 h and surviving cells were counted after plating microdiluted samples. No viable *E. coli* bacteria were observed after treatment with 150  $\mu$ g mL<sup>-1</sup> of MoSe<sub>2</sub>/T<sub>20</sub>, and the killing efficiency increased with increasing concentration (Figure 4e). Furthermore, at lower concentrations of MoSe<sub>2</sub>/T<sub>20</sub>, higher killing efficiency was observed for NDM *E. coli* strains as compared to KPC *E. coli* strains, as shown in Figure 4e. At 100  $\mu$ g mL<sup>-1</sup>, MoSe<sub>2</sub>/T<sub>20</sub> showed 99.98% and 99.8% cell killing for the NDM strains, whereas 99.5% cell killing was observed for the KPC strain.

We then evaluated the antibacterial efficiency of  $MoSe_2/T_{20}$  on additional nosocomial MDR clinical isolates. We chose two

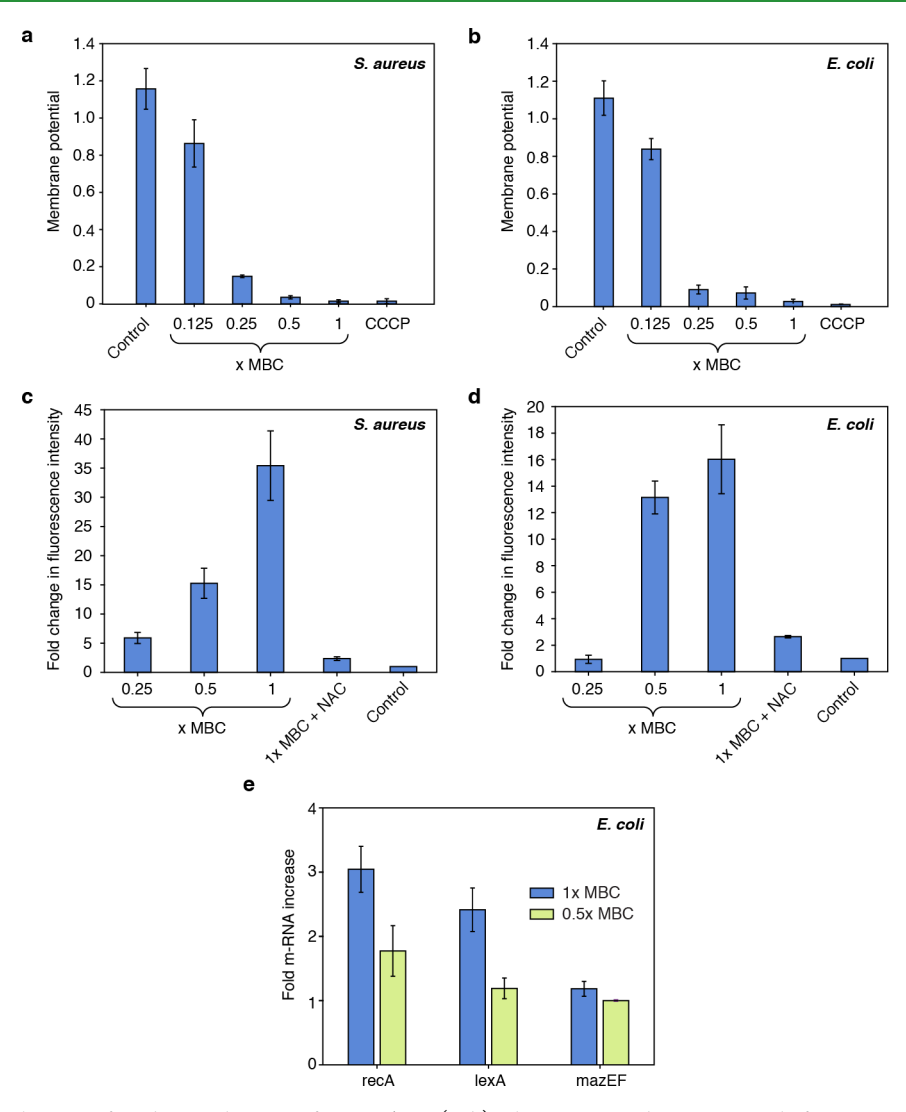


Figure 6. Analysis of mechanism of antibacterial action of  $MoSe_2/T_{20}$ . (a, b) Change in membrane potential after interactions of  $MoSe_2/T_{20}$  with (a) *S. aureus* and (b) *E. coli*. (c, d) Oxidative stress generated in (c) *S. aureus* and (d) *E. coli* after interactions with  $MoSe_2/T_{20}$ . (e) Fold change in mRNA expression after interactions with  $MoSe_2/T_{20}$  in *E. coli*.

well-known Gram-positive clinical strains, methicillin-resistant Staphylococcus aureus (MRSA) and vancomycin-resistant Enterococcus faecalis (VRE). MRSA, which is responsible for 25% to 50% of nosocomial infections, expresses the mecA gene that provides it with resistance to a broad spectrum of  $\beta$ -lactam antibiotics. VRE, which causes urinary tract infections, is resistant to all  $\beta$ -lactam antibiotics and last resort antibiotics for treating vancomycin. After 4 h of treatment, 75  $\mu$ g mL<sup>-1</sup> MoSe<sub>2</sub>/T<sub>20</sub> successfully eliminated 10<sup>7</sup> orders of VRE and MRSA (Figure 4f). We examined the efficiency of  $MoSe_2/T_{20}$ against the Gram-negative strains Klebsiella pneumoniae, Acinetobacter baumannii, Pseudomonas aeruginosa, and Enterobacter cloacae (Figure 4g). Antibiotic resistance conducted by ATCC on P. aeruginosa and A. baumannii strains demonstrated resistance to 15 and 31 different classes of antibiotics, respectively, whereas E. cloacae and K. pneumoniae demonstrated resistance to 36 different classes of antibiotics. After 4 h of treatment, 75  $\mu$ g mL<sup>-1</sup> of MoSe<sub>2</sub>/T<sub>20</sub> successfully eradicated all the four Gram-negative MDR strains. The successful eradication of these strains demonstrates that MoSe<sub>2</sub>/T<sub>20</sub> holds potential as one of the next-generation broad-spectrum

antibacterial candidates for combating these drug-resistant bacteria.

Mechanistic Studies of Antibacterial Activity of MoSe<sub>2</sub>/ssDNA. We carried out a series of experiments to determine the mechanisms by which the MoSe<sub>2</sub>/T<sub>20</sub> achieves antibacterial activity. First, we used scanning electron microscopy (SEM) and TEM imaging studies to investigate the effect of MoSe<sub>2</sub>/T<sub>20</sub> interactions on the cell morphology of the Gram-positive MRSA and Gram-negative A. baumannii bacteria, as shown in Figure 5. SEM images of untreated MRSA and A. baumannii samples showed no significant morphological changes and TEM images of them showed the cytoplasm inside them was intact (Figure 5a, d). After treatment with  $MoSe_2/T_{20}$  at 0.5× MBC (37.5  $\mu g$  mL<sup>-</sup>1), the SEM showed formation of small blob-like structures (Figure 5b, e), which increase in concentration at  $1 \times$  MBC (75  $\mu$ g/mL) (Figure 5c, f). The formation of small blobs is attributed to the sharp edges of the MoSe<sub>2</sub>/T<sub>20</sub> causing breakdown of the cell membrane. TEM images of MRSA and A. baumannii after  $MoSe_2/T_{20}$  interaction at both 0.5× MBC and 1× MBC concentrations show MoSe<sub>2</sub> nanosheets surrounding and penetrating the cell membranes of the bacteria. In both types of bacteria, TEM images show the presence of void spaces in the cytoplasm at  $0.5\times$  MBC, which become much larger at  $1\times$  MBC. The formation of small grooves in the cellular membrane leads to disruption and leakage of the cytoplasm. The nature of damage to the cellular membrane and cytoplasm is identical for both Gram-positive and Gram-negative bacteria, which further supports the broad-spectrum antibacterial nature of these  $MoSe_2/T_{20}$  materials. SEM and TEM images of *E. coli* cells are shown in Figure S4, and exhibit similar disruption of the cell membranes and formation of internal voids with  $MoSe_2/T_{20}$  treatment.

The microscopic analysis of MoSe<sub>2</sub>/T<sub>20</sub>-treated bacteria indicate that the MoSe2 flakes caused severe damage to the cell membranes, which are then unable to hold the turgor pressure of the cytoplasm so that it leaks out. The observed effect is consistent with other reports of the antibacterial mechanism of 2D nanomaterials, which physically disrupt cell membranes by their atomically sharp edges and by membrane depolarization caused by the relatively hydrophobic nature of MoSe<sub>2</sub> surface. 11,47-50,61,62 Previous theoretical and experimental studies of antibacterial mechanisms of graphene-based nanomaterials have shown that they act like blades penetrating through bacterial cell membranes, causing physical damage, and leading to leakage of cytoplasm. On the basis of previous studies, we also hypothesize that the presence of ssDNA on the MoSe<sub>2</sub> surfaces increases their hydrophilicity, which encourages them to make contact with the outer surfaces of the bacteria.<sup>32</sup> Once in close proximity, the sharp edges of the MoSe<sub>2</sub>/T<sub>20</sub>, which are more readily exposed as a result of the conformal ssDNA coating, are better able to interfere with the membrane to trigger cell death. We note that these imaging studies show that the primary nanomaterial present are the MoSe<sub>2</sub> nanosheets without the presence of any Se nanoparticles, which also exhibit antibacterial activity on their own. 63,64

To confirm our hypothesis that the deformities in the cells observed in Figure 5 may result from membrane depolarization caused by the interaction of MoSe<sub>2</sub>/T<sub>20</sub> with the bacteria, we conducted a membrane potential assay. We used the probe 3,3'-diethyloxacarbocyanine iodide (DiOC<sub>2</sub>), which is a cyanine dye that permeates the cell membrane exhibiting green fluorescence, and undergoes aggregation in polarized cells leading to fluorescence shifting from green to red. We evaluated the change in membrane potential after MoSe<sub>2</sub>/T<sub>20</sub> interactions on two different strains of bacteria, Gram-positive S. aureus and Gram-negative E. coli. For the membrane potential assay, we treated the bacteria at four different concentrations of  $MoSe_2/T_{20}$ : 1× MBC, 0.5× MBC, 0.25× MBC, and 0.125× MBC. The results of this assay are shown in Figure 6a and b. We used carbonyl cyanide 3-chlorophenylhydrazone (CCCP), a known membrane ionophore, as a positive control for the membrane potential assay. With increasing MoSe<sub>2</sub>/T<sub>20</sub> concentrations, the fluorescence shifts toward the green channel and leads to a lowering of the red/green fluorescence intensity ratio. The change in fluorescence intensity ratio indicates that interactions with the MoSe<sub>2</sub>/T<sub>20</sub> nanosheets indeed trigger depolarization of the cell membrane.

The induction of oxidative stress was evaluated using the fluorogenic probe CellROX for the same Gram-positive *S. aureus* and Gram-negative *E. coli* at three different concentrations of  $MoSe_2/T_{20}$ : 1× MBC, 0.5× MBC, and 0.25× MBC. The dye in this test exhibits bright green fluorescence when it is oxidized by the presence of reactive oxygen species (ROS)

and subsequently binds to cellular DNA. This suggests the ROS generated stress was intracellular and the fluorescence observed in the results in Figure 6c and d indicate more oxidative stress with increasing concentrations of  $MoSe_2/T_{20}$ . At  $1\times MBC$ ,  $MoSe_2/T_{20}$  induces 42-fold and 16-fold higher oxidative stress for *S. aureus* and *E. coli*, respectively, compared to untreated samples. Upon the addition of the antioxidant N-acetylcysteine (NAC) at  $1\times MBC$  of  $MoSe_2/T_{20}$  concentration, the oxidative stress decreases by 19-fold and 6-fold in *S. aureus* and *E. coli*, respectively, which further demonstrates the generation of cellular oxidative stress.

Analysis of TMDCs in the literature have shown that their antibacterial efficiency can be attributed to both ROSdependent and -independent stress. 26,27,31,65 TMDCs are capable of producing many scavenger radicals, but peroxide has been established as the dominant species.<sup>26</sup> It has also been reported that MoSe<sub>2</sub> among other TMDCs produced hydroxyl radicals and singlet oxygen derived from superoxide anions  $(O^{\bullet-2})$ , which contribute toward the generation of ROSmediated stress causing cell death.<sup>31</sup> Also, the oxidation capacity increases with increasing the concentration of the antimicrobial material, which is consistent with our observations.<sup>27</sup> It has also been observed that 2D TMDCs are capable of inducing superoxide anion-independent oxidative stress.<sup>27</sup> Thus, we hypothesize that our  $MoSe_2/T_{20}$  material similarly is capable of both ROS-dependent and -independent stress, which leads to enhanced antibacterial activity.

The impact of membrane potential and oxidative stress on DNA damage in S. aureus and E. coli were evaluated next. Damage to DNA generally triggers programmed cell death (PCD). There are two well-known pathways for programmed cell death, the RecA and mazEF pathways. The mazEF pathways refers to toxin-antitoxin module of bacteria. mazF genes generally encode for a toxic endoribonuclease protein MazF, which quickly degrades mRNA, whereas mazE genes lead to secretion of the antitoxin mazE, which neutralizes the effect of MazF. Under stressful conditions, MazE is quickly degraded by ClpPA serine protease, which leads to the presence of higher toxic protein, and in turn cell death. The SOS response pathway refers to inducible pathways that are responsible for DNA repair. There are two key proteins which is responsible for this SOS response pathway: repressor LexA and inducer RecA. In the absence of DNA damage, the LexA dimer binds to the palindromic sequence of the DNA SOS box, inhibiting expression of RecA genes. When there is DNA damage, the RecA pathway is activated leading to self-cleavage of LexA and activation of RecA pathways, which leads to cell death. We studied the programmed cell death pathways of E. coli after interaction with 0.5× MBC and 1× MBC of MoSe<sub>2</sub>/ T<sub>20</sub>, which showed 2-fold and 3-fold increase in mRNA expression of RecA levels, whereas mazEF levels were essentially unchanged for both the tested concentrations. These studies clearly demonstrate that MoSe<sub>2</sub>/T<sub>20</sub> triggers two PCD pathways in bacterial cells to induce cell death.

On the basis of all the mechanistic studies described above, we believe the antibacterial activity of  $MoSe_2/T_{20}$  can be summarized as a three-step process. First, the sharp edges of  $MoSe_2$  insert into the bacterial cell membranes, causing ruptures. These ruptures lead to depolarization of the cell membrane. The change in the membrane potential then induces oxidative stress, causing damage to the cellular machinery and in turn cell death.

## DISCUSSION

The MoSe<sub>2</sub>/T<sub>20</sub> has excellent broad-spectrum antibacterial performance after relatively short incubation times and low toxicity (see detailed comparisons with many other 2D materials and nanomaterials in Figure S5 and Tables S1 and S2). Our system achieved a roughly six log order reduction in bacterial cells, which was significantly better than most other systems we reviewed, and was only matched by Ag<sup>+</sup>-Cys-MoS<sub>2</sub>, WS<sub>2</sub>/SDS, Se nanoparticles, and rGO and GO. However, compared to these nanomaterials, the MoSe<sub>2</sub>/ T<sub>20</sub> has better mammalian cell viability and/or faster antibacterial activity rate. We used a 4 h incubation time in our work, while many other reports had longer incubation times. The overall MBC values we find are generally comparable to other systems in the literature. However, our MoSe<sub>2</sub>/T<sub>20</sub> system is also effectively a single active component rather than a synergistic system like Ag<sup>+</sup>-Cys-MoS<sub>2</sub><sup>25</sup> and does not use any further additives that are themselves antibacterial, such as cationic polymers, surfactants, 26 lysozyme, 64 silver ions, 25 or chitosan, 18,23 so that it is less cytotoxic and thus more suitable for biological applications. Furthermore, unlike previously developed antibacterial systems, MoSe<sub>2</sub>/T<sub>20</sub> demonstrates excellent broad-spectrum antibacterial action. Overall, the combination of these performance metrics-highly effective killing of both Gram-positive and Gram-negative bacteria, eradication of MDR bacteria, reasonable MBC values at short incubation times, and high mammalian cell viabilitymake MoSe<sub>2</sub>/T<sub>20</sub> a very promising antibacterial material.

# CONCLUSION

Using short, synthetic ssDNA sequences, we have successfully prepared stable dispersions of 2D TMDCs in aqueous solutions and demonstrated the remarkable antibacterial performance of MoSe<sub>2</sub>/T<sub>20</sub>. Exfoliation of few-layer TMDC nanosheets was confirmed using optical absorbance and TEM and AFM imaging. Concentration measurements using ICP-MS identified MoSe<sub>2</sub> as the TMDC most effectively dispersed using synthetic ssDNA. Owing to the biocompatibility of the ssDNA coating, we studied the effect of the MoSe<sub>2</sub> nanosheets encapsulated by T<sub>20</sub> ssDNA against human and bacterial cells. While no toxicity was observed against a human cell line, we observed very potent bactericidal activity for the MoSe<sub>2</sub>/T<sub>20</sub> nanosheets against multiple strains of Gram-negative and Gram-positive bacteria including highly drug resistant strains. In side-by-side comparisons, the bactericidal efficiency of MoSe<sub>2</sub>/T<sub>20</sub> nanosheets exceeded that of GO, which is the most widely studied 2D antibacterial material, by more than 1000fold. MoSe<sub>2</sub> prepared using genomic DNA or with Pluronic F77 coating were much less effective at eliminating the bacteria, demonstrating the critical importance of an optimized, conformal ssDNA coating for enhanced antibacterial activity. The effective conformal coating of the T<sub>20</sub> ssDNA sequence was also confirmed using MD simulations. Imaging studies of both MRSA and A. baumannii cells treated with the MoSe<sub>2</sub>/T<sub>20</sub> revealed that the ultrathin nanosheets aggressively interact with the cell walls of the bacteria, depolarizing and rupturing the cell membrane to induce cell death. Crucially, MoSe<sub>2</sub>/T<sub>20</sub> successfully eradicated clinical isolates of highly drug resistant strains, demonstrating its potential as a broadspectrum antibacterial material against bacteria that have developed resistance to most other antibiotic drugs.

These results not only demonstrate that  $MoSe_2/T_{20}$  can exhibit antibiotic-like activity against MDR bacteria but also emphasizes the importance of employing optimized encapsulation agents to enhance the effectiveness of 2D nanosheets. In particular, the use of a conformal ssDNA coating suggests that an array of other biocompatible biomolecules can be interfaced with intrinsically antimicrobial 2D nanomaterials to generate effective new tools to combat the growing threat of antimicrobial drug resistance.

#### METHODS

**Solution-Phase Dispersion of TMDCs in ssDNA.** In a typical experiment, TMDC powder was added to a 5 mL aqueous solution containing 1 mg of single-stranded DNA (Integrated DNA Technologies). MoSe<sub>2</sub> and WSe<sub>2</sub> bulk powder (Sigma-Aldrich) at a mass of 200 mg was used for each dispersion, while a lower mass of 100 mg of MoS<sub>2</sub> and WS<sub>2</sub> (Sigma-Aldrich) led to higher concentration dispersions for these compounds. The resulting mixture was ultrasonicated with a 13 mm tip at a power level of 12 W for 2 h (Branson Digital Sonifier 450D). After ultrasonication, the sample was centrifuged at 5000g for 5 min followed by 21 000g for 1 min to remove the remaining bulk material. The supernatant of ssDNA-encapsulated TMDC nanosheets was then carefully decanted for study.

TEM Analysis of ssDNA-Dispersed TMDC Nanosheets. The samples were prepared by dropping 6  $\mu$ L of dispersed solution of TMDCs onto holey carbon copper grids and imaged using a Phillips CM-12 TEM at 80 kV acceleration voltage.

AFM Analysis of ssDNA-Dispersed TMDC Nanosheets. Highly oriented pyrolytic graphite (HOPG) substrates (SPI, Inc.) were freshly cleaved using adhesive tape. Then the dispersions of nanomaterials were spin-coated onto the substrates at 2500 rpm. The spin coated samples were annealed in vacuum with 200 sccm of ultrahigh purity argon gas flow at 300 °C for 3 h to remove organic residues. AFM images were taken using a Multimode V system (Bruker Inc.) in ScanAsyst mode with ScanAsyst-Air tips and image processing was conducted using Gwyddion. 66

Antibacterial Studies. The antibacterial activity of MoSe<sub>2</sub>/T<sub>20</sub> was studied using wild type *E. coli* strain MG1655 (ATCC, 700926), three *E. coli* MDR strains (ATCC, BAA-2340; ATCC, BAA-2469; and ATCC, BAA-2471), *Staphylococcus aureus* (ATCC, 29213), methicillin-resistant *Staphylococcus aureus* (ATCC, BAA 1720), *Pseudomonas aeruginosa* (ATCC, BAA 2113), *Klebsiella pneumoniae* (ATCC, BAA 2342), vancomycin-resistant *Enterococcus faecalis* (ATCC, 51299), *Acinetobacter baumannii* (ATCC, BAA 1797), and *Enterobacter cloacae* (ATCC, BAA 2468).

LB medium (Sigma-Aldrich) and LB agar (Sigma-Aldrich) were used to grow E. coli strain MG1655. TSB broth (Sigma-Aldrich) and TSB agar (Sigma-Aldrich) were used to grow S. aureus, methicillinresistant S. aureus, P. aeruginosa, and A. baumannii, whereas vancomycin-resistant E. faecalis were grown in BHB broth (Sigma-Aldrich) and BHB agar (Sigma-Aldrich) in the presence of 4  $\mu$ g/mL of vancomycin. MHB broth (Sigma-Aldrich) and MHB agar (Sigma-Aldrich) were used to grow K. pneumoniae. Single colonies were picked from agar plates and allowed to grow overnight in 5 mL of culture medium. Then, each sample was diluted 100 times in medium and allowed to grow until it reached 0.3 OD. Cultures were centrifuged at 2000 rpm for 10 min, and pellets were washed three times in phosphate buffer saline (PBS, Sigma-Aldrich) to remove medium constituents. Finally, cell pellets were redispersed in autoclaved water and diluted to a cell concentration of  $\bar{1}0^7$  CFU/ mL. Bacteria at concentrations of 107 CFU/mL were incubated with different concentrations of nanomaterials (40–150  $\mu$ g/mL) for 4 h. After incubation, bacteria were plated in agar plates using serial dilution method and allowed to grow overnight.

Mammalian Cell Viability of MoSe<sub>2</sub>/ssDNA. For determination of mammalian cell viability in the presence of MoSe<sub>2</sub>/T<sub>20</sub>, we used the A549 epithelial cell line and performed the MTT assay (kit from

Roche), which is used to measure cellular metabolic activity as an indicator of cell viability. In this colorimetric assay, yellow tetrazolium salt (3-(4,5-dimethylthiazol-2-yl)-2,5-diphenyltetrazolium bromide) or MTT is reduced to purple formazan crystals by metabolically active cells. Cells were seeded in 96-well microplates at a density of 1  $\times$  10<sup>5</sup> cells mL<sup>-1</sup> in a 200- $\mu$ L volume with F-12K medium. After 24 h of cell attachment at 37  $^{\circ}$ C in the presence of 5% CO<sub>2</sub>, the plates were washed with DPBS and the MoSe<sub>2</sub>/T<sub>20</sub> at different concentration were incubated with the mammalian cells for 72 h at 37 °C in the presence of 5% CO<sub>2</sub>. Then, the wells were washed three times with 1× DPBS to remove any unattached cells. To check the viability of the attached cells after the incubation period, 100  $\mu$ L of 0.5 mg mL<sup>-1</sup> final concentration of MTT solution in F-12K medium was added to each well. The 96-well microplate was then incubated at 37 °C in the presence of 5% CO<sub>2</sub> for 4 h. At the end of the incubation, 100  $\mu$ L of the solubilization solution (10% SDS in 0.01 M HCl) was added in each well and was allowed to stand overnight. 150  $\mu L$  of supernatant was collected in a fresh 96-well microplate and absorbance at 570 nm was collected using a microplate reader. Mammalian cells treated with just F-12K without any MoSe<sub>2</sub>/T<sub>20</sub> were measured as control samples. The absorbance of F-12K was subtracted from all the above values as blank. All the experiments were performed in triplicate.

TEM and SEM Analysis of Bacteria. For TEM imaging, samples were initially fixed with 2.5% glutaraldehyde overnight at 4 °C and pelleted into 0.8% aggregate to form dense cell aggregates. The cell pellet was treated for 2 h with 1% osmium tetraoxide in DPBS, followed by washing with deionized water and en-block stained overnight at 4 °C with aqueous 0.5% uranyl acetate. The cell pellet was dehydrated in series in a graded acetone series. The sample was sectioned and post-stained using 2% uranyl acetate in 50% ethanol solution and Sato's lead citrate for 3–4 min. Images were acquired using Phillips CM-12 TEM operated at 80 kV using a Gatan model 791 side-mount CCD camera.

For SEM imaging, samples were initially fixed using 2.5% glutaraldehyde at 4 °C, followed by washing with DPBS. The samples were postfixed with 1% osmium tetraoxide in DPBS, followed by washing with deionized water and dehydration in a graded ethanol series. The samples were critically dried, sputtered coated with gold—palladium and images were captured using a JEOL JSM6300 SEM operated at 15 kV.

**Membrane Potential Assay.** The membrane potentials of bacteria were determined using a Baclight membrane potential kit (Invitrogen) following the manufacturer's protocol. Briefly, bacteria were harvested at mid log phase and diluted to  $\sim\!10^6$  CFU/mL in autoclaved water. The bacteria were treated with different concentrations of MoSe<sub>2</sub>/T<sub>20</sub> (1× MBC, 0.5× MBC, 0.25× MBC, and 0.125× MBC) for 4 h. A fully depolarized sample was prepared on addition of 5 mM proton ionophore, carbonyl cyanide 3-chlorophenylhydrazone (CCCP). After treatment, samples were incubated with 30 mM DiOC<sub>2</sub> for 1 h. The membrane potential was determined using a Stratedigm S1300EXi cell analyzer equipped with A600 high-throughput autosampler as the ratio of cells exhibiting red fluorescence to cells exhibiting green fluorescence. Cell populations were gated based on measurements from untreated (polarized) and CCCP-treated (depolarized) samples.

ROS Production Assay. E. coli and S. aureus were inoculated in LB medium and TSB medium, respectively, harvested at mid log phase, and diluted to  $\sim\!10^6$  cells in autoclaved water. The samples were treated with different concentrations of MoSe $_2/T_{20}$  (1× MBC, 0.5× MBC, 0.25× MBC) for 4 h. After incubation, cells were stained using the CellROX orange reagent (Invitrogen) following the manufacturer's protocol. Briefly, samples were stained with 750 mM of CellROX orange reagent, and samples was analyzed using Stratedigm S1300EXi cell analyzer equipped with an A600 high-throughput autosampler and mCherry fluorescence output was used to determine the oxidative stress of the cells.

# ASSOCIATED CONTENT

# **Supporting Information**

The Supporting Information is available free of charge at https://pubs.acs.org/doi/10.1021/acsami.0c22941.

Zeta potentials of TMDC dispersions, cell viability study with human epithelial cells, growth media bacterial viability comparison, additional electron microscopy data for  $E.\ coli$  exposed to  $MoSe_2/T_{20}$ , plots of log reduction bacteria for different literature studies and our work, and tables of detailed comparisons of different antimicrobial nanomaterials from literature and our work (PDF)

#### AUTHOR INFORMATION

# **Corresponding Authors**

Alexander A. Green — Biodesign Center for Molecular Design and Biomimetics, The Biodesign Institute and School of Molecular Sciences, Arizona State University, Tempe, Arizona 85287, United States; Department of Biomedical Engineering, Boston University, Boston, Massachusetts 02215, United States; orcid.org/0000-0003-2058-1204; Email: aagreen@bu.edu

Qing Hua Wang — Materials Science and Engineering, School for Engineering of Matter, Transport and Energy, Arizona State University, Tempe, Arizona 85287, United States;
orcid.org/0000-0002-7982-7275; Email: qhwang@asu.edu

#### **Authors**

Abhishek Debnath — Biodesign Center for Molecular Design and Biomimetics, The Biodesign Institute and School of Molecular Sciences, Arizona State University, Tempe, Arizona 85287, United States

Sanchari Saha — Biodesign Center for Molecular Design and Biomimetics, The Biodesign Institute and School of Molecular Sciences, Arizona State University, Tempe, Arizona 85287, United States

Duo O. Li – Materials Science and Engineering, School for Engineering of Matter, Transport and Energy, Arizona State University, Tempe, Arizona 85287, United States

Ximo S. Chu — Materials Science and Engineering, School for Engineering of Matter, Transport and Energy, Arizona State University, Tempe, Arizona 85287, United States;
ocid.org/0000-0003-2308-6268

Zachary W. Ulissi — Department of Chemical Engineering, Carnegie Mellon University, Pittsburgh, Pennsylvania 15213, United States; orcid.org/0000-0002-9401-4918

Complete contact information is available at: https://pubs.acs.org/10.1021/acsami.0c22941

#### **Notes**

The authors declare no competing financial interest.

# ACKNOWLEDGMENTS

We gratefully acknowledge the use of facilities at the LeRoy Eyring Center for Solid State Science at Arizona State University and Prof. Hao Yan for use of his AFM. A.A.G. and Q.H.W. acknowledge support from NSF Grant DMR-1610153 and ASU startup funds. Q.H.W. acknowledges NSF grant DMR-1906030. A.A.G. acknowledges an Alfred P. Sloan Research Fellowship (FG-2017-9108).

## REFERENCES

- (1) Davies, J.; Davies, D. Origins and Evolution of Antibiotic Resistance. *Microbiol. Mol. Biol. Rev.* **2010**, *74*, 417–433.
- (2) Centers for Disease Control and Prevention. The Growing Threat of Multidrug-Resistant Gonorrhea. MMWR Morb. Mortal Wkly. Rep. 2013, 62, 103–106.
- (3) van Duin, D.; Paterson, D. L. Multidrug-Resistant Bacteria in the Community: Trends and Lessons Learned. *Infect. Dis. Clin. North Am.* **2016**, 30, 377–390.
- (4) Blair, J. M. A.; Webber, M. A.; Baylay, A. J.; Ogbolu, D. O.; Piddock, L. J. V. Molecular Mechanisms of Antibiotic Resistance. *Nat. Rev. Microbiol.* **2015**, *13*, 42–51.
- (5) Sun, W.; Wu, F.-G. Two-Dimensional Materials for Antimicrobial Applications: Graphene Materials and Beyond. *Chem. Asian J.* **2018**, *13*, 3378–3410.
- (6) Miao, H.; Teng, Z.; Wang, C.; Chong, H.; Wang, G. Recent Progress in Two-Dimensional Antimicrobial Nanomaterials. *Chem. Eur. J.* **2019**, 25, 929–944.
- (7) Zheng, J.; Li, J.; Zhang, L.; Chen, X.; Yu, Y.; Huang, H. Post-Graphene 2D Materials-Based Antimicrobial Agents: Focus on Fabrication Strategies and Biosafety Assessments. *J. Mater. Sci.* **2020**, *55*, 7226–7246.
- (8) Begum, S.; Pramanik, A.; Davis, D.; Patibandla, S.; Gates, K.; Gao, Y.; Ray, P. C. 2D and Heterostructure Nanomaterial Based Strategies for Combating Drug-Resistant Bacteria. *ACS Omega* **2020**, *5*, 3116–3130.
- (9) Hui, L.; Piao, J.-G.; Auletta, J.; Hu, K.; Zhu, Y.; Meyer, T.; Liu, H.; Yang, L. Availability of the Basal Planes of Graphene Oxide Determines Whether It Is Antibacterial. *ACS Appl. Mater. Interfaces* **2014**, *6*, 13183–13190.
- (10) Akhavan, O.; Ghaderi, E. Toxicity of Graphene and Graphene Oxide Nanowalls Against Bacteria. ACS Nano 2010, 4, 5731-5736.
- (11) Hu, W.; Peng, C.; Luo, W.; Lv, M.; Li, X.; Li, D.; Huang, Q.; Fan, C. Graphene-Based Antibacterial Paper. ACS Nano 2010, 4, 4317–23.
- (12) Liu, S. B.; Zeng, T. H.; Hofmann, M.; Burcombe, E.; Wei, J.; Jiang, R. R.; Kong, J.; Chen, Y. Antibacterial Activity of Graphite, Graphite Oxide, Graphene Oxide, and Reduced Graphene Oxide: Membrane and Oxidative Stress. *ACS Nano* **2011**, *5*, 6971–6980.
- (13) Ristic, B. Z.; Milenkovic, M. M.; Dakic, I. R.; Todorovic-Markovic, B. M.; Milosavljevic, M. S.; Budimir, M. D.; Paunovic, V. G.; Dramicanin, M. D.; Markovic, Z. M.; Trajkovic, V. S. Photodynamic Antibacterial Effect of Graphene Quantum Dots. *Biomaterials* **2014**, *35*, 4428–35.
- (14) Gurunathan, S.; Woong Han, J.; Abdal Daye, A.; Eppakayala, V.; Kim, J.-h. Oxidative Stress-Mediated Antibacterial Activity of Graphene Oxide and Reduced Graphene Oxide in Pseudomonas aeruginosa. *Int. J. Nanomed.* **2012**, *7*, 5901–5914.
- (15) Liu, S.; Hu, M.; Zeng, T. H.; Wu, R.; Jiang, R.; Wei, J.; Wang, L.; Kong, J.; Chen, Y. Lateral Dimension-Dependent Antibacterial Activity of Graphene Oxide Sheets. *Langmuir* **2012**, *28*, 12364–12372.
- (16) Kurantowicz, N.; Sawosz, E.; Jaworski, S.; Kutwin, M.; Strojny, B.; Wierzbicki, M.; Szeliga, J.; Hotowy, A.; Lipińska, L.; Koziński, R.; Jagiełło, J.; Chwalibog, A. Interaction of Graphene Family Materials with Listeria monocytogenes and Salmonella enterica. *Nanoscale Res. Lett.* 2015, 10, 23.
- (17) Liu, L.; Liu, J.; Wang, Y.; Yan, X.; Sun, D. D. Facile Synthesis of Monodispersed Silver Nanoparticles on Graphene Oxide Sheets with Enhanced Antibacterial Activity. *New J. Chem.* **2011**, *35*, 1418–1423.
- (18) Ray Chowdhuri, A.; Tripathy, S.; Chandra, S.; Roy, S.; Sahu, S. K. A ZnO Decorated Chitosan—Graphene Oxide Nanocomposite Shows Significantly Enhanced Antimicrobial Activity with ROS Generation. *RSC Adv.* **2015**, *5*, 49420–49428.
- (19) Li, J. H.; Wang, G.; Zhu, H. Q.; Zhang, M.; Zheng, X. H.; Di, Z. F.; Liu, X. Y.; Wang, X. Antibacterial Activity of Large-Area Monolayer Graphene Film Manipulated by Charge Transfer. *Sci. Rep.* **2015**, *4*, 4359.

- (20) Han, F.; Lv, S.; Li, Z.; Jin, L.; Fan, B.; Zhang, J.; Zhang, R.; Zhang, X.; Han, L.; Li, J. Triple-Synergistic 2D Material-Based Dual-Delivery Antibiotic Platform. NPG Asia Mater. 2020, 12, 15.
- (21) Han, W.; Wu, Z.; Li, Y.; Wang, Y. Graphene Family Nanomaterials (GFNs)—Promising Materials for Antimicrobial Coating and Film: A Review. *Chem. Eng. J.* **2019**, 358, 1022–1037.
- (22) Kurapati, R.; Muzi, L.; De Garibay, A. P. R.; Russier, J.; Voiry, D.; Vacchi, I. A.; Chhowalla, M.; Bianco, A. Enzymatic Biodegradability of Pristine and Functionalized Transition Metal Dichalcogenide MoS<sub>2</sub> Nanosheets. *Adv. Funct. Mater.* **2017**, 27, 1605176.
- (23) Roy, S.; Mondal, A.; Yadav, V.; Sarkar, A.; Banerjee, R.; Sanpui, P.; Jaiswal, A. Mechanistic Insight into the Antibacterial Activity of Chitosan Exfoliated MoS<sub>2</sub> Nanosheets: Membrane Damage, Metabolic Inactivation, and Oxidative Stress. ACS Appl. Bio Mater. 2019, 2, 2738–2755.
- (24) Pandit, S.; Karunakaran, S.; Boda, S. K.; Basu, B.; De, M. High Antibacterial Activity of Functionalized Chemically Exfoliated MoS<sub>2</sub>. ACS Appl. Mater. Interfaces **2016**, *8*, 31567–31573.
- (25) Cao, F.; Ju, E.; Zhang, Y.; Wang, Z.; Liu, C.; Li, W.; Huang, Y.; Dong, K.; Ren, J.; Qu, X. An Efficient and Benign Antimicrobial Depot Based on Silver-Infused MoS<sub>2</sub>. ACS Nano **2017**, 11, 4651–4659.
- (26) Karunakaran, S.; Pandit, S.; Basu, B.; De, M. Simultaneous Exfoliation and Functionalization of 2H-MoS2 by Thiolated Surfactants: Applications in Enhanced Antibacterial Activity. *J. Am. Chem. Soc.* **2018**, *140*, 12634–12644.
- (27) Yang, X.; Li, J.; Liang, T.; Ma, C.; Zhang, Y.; Chen, H.; Hanagata, N.; Su, H.; Xu, M. Antibacterial Activity of Two-Dimensional MoS<sub>2</sub> Sheets. *Nanoscale* **2014**, *6*, 10126–10133.
- (28) Liu, C.; Kong, D. S.; Hsu, P. C.; Yuan, H. T.; Lee, H. W.; Liu, Y. Y.; Wang, H. T.; Wang, S.; Yan, K.; Lin, D. C.; Maraccini, P. A.; Parker, K. M.; Boehm, A. B.; Cui, Y. Rapid Water Disinfection Using Vertically Aligned MoS<sub>2</sub> Nanofilms and Visible Light. *Nat. Nanotechnol.* **2016**, *11*, 1098–1104.
- (29) Liu, X.; Duan, G.; Li, W.; Zhou, Z.; Zhou, R. Membrane Destruction-Mediated Antibacterial Activity of Tungsten Disulfide (WS<sub>2</sub>). RSC Adv. 2017, 7, 37873–37880.
- (30) Navale, G. R.; Rout, C. S.; Gohil, K. N.; Dharne, M. S.; Late, D. J.; Shinde, S. S. Oxidative and Membrane Stress-Mediated Antibacterial Activity of WS<sub>2</sub> and rGO-WS<sub>2</sub> Nanosheets. *RSC Adv.* **2015**, *5*, 74726–74733.
- (31) Kim, T. I.; Kim, J.; Park, I.-J.; Cho, K.-O.; Choi, S.-Y. Chemically Exfoliated 1T-Phase Transition Metal Dichalcogenide Nanosheets for Transparent Antibacterial Applications. 2D Mater. **2019**, *6*, No. 025025.
- (32) Bang, G. S.; Cho, S.; Son, N.; Shim, G. W.; Cho, B.-K.; Choi, S.-Y. DNA-Assisted Exfoliation of Tungsten Dichalcogenides and Their Antibacterial Effect. ACS Appl. Mater. Interfaces 2016, 8, 1943—1950
- (33) Rasool, K.; Helal, M.; Ali, A.; Ren, C. E.; Gogotsi, Y.; Mahmoud, K. A. Antibacterial Activity of  ${\rm Ti_3C_2T_x}$  MXene. *ACS Nano* **2016**, 10, 3674–3684.
- (34) Arabi Shamsabadi, A.; Sharifian Gh, M.; Anasori, B.; Soroush, M. Antimicrobial Mode-of-Action of Colloidal  $Ti_3C_2T_x$  MXene Nanosheets. *ACS Sustainable Chem. Eng.* **2018**, *6*, 16586–16596.
- (35) Rasool, K.; Mahmoud, K. A.; Johnson, D. J.; Helal, M.; Berdiyorov, G. R.; Gogotsi, Y. Efficient Antibacterial Membrane based on Two-Dimensional Ti<sub>3</sub>C<sub>2</sub>T<sub>x</sub> (MXene) Nanosheets. *Sci. Rep.* **2017**, 7, 1598.
- (36) Rajavel, K.; Shen, S.; Ke, T.; Lin, D. Achieving High Bactericidal and Antibiofouling Activities of 2D Titanium Carbide  $(Ti_3C_2T_x)$  by Delamination and Intercalation. 2D Mater. **2019**, 6, No. 035040.
- (37) Fan, X.; Yang, F.; Huang, J.; Yang, Y.; Nie, C.; Zhao, W.; Ma, L.; Cheng, C.; Zhao, C.; Haag, R. Metal—Organic-Framework-Derived 2D Carbon Nanosheets for Localized Multiple Bacterial Eradication and Augmented Anti-infective Therapy. *Nano Lett.* **2019**, 19, 5885–5896.

- (38) Becker, M. L.; Fagan, J. A.; Gallant, N. D.; Bauer, B. J.; Bajpai, V.; Hobbie, E. K.; Lacerda, S. H.; Migler, K. B.; Jakupciak, J. P. Length-Dependent Uptake of DNA-Wrapped Single-Walled Carbon Nanotubes. *Adv. Mater.* **2007**, *19*, 939–945.
- (39) D'yachkov, E. P.; Dolin, S. P.; D'yachkov, P. N. Interaction of Single-Stranded DNA with Carbon Nanotubes According to the Molecular Docking Method. *Dokl. Phys. Chem.* **2008**, 423, 297–301.
- (40) Dovbeshko, G. I.; Repnytska, O. P.; Obraztsova, E. D.; Shtogun, Y. V. DNA Interaction with Single-Walled Carbon Nanotubes: A SEIRA Study. *Chem. Phys. Lett.* **2003**, 372, 432–437.
- (41) Gladchenko, G. O.; Karachevtsev, M. V.; Leontiev, V. S.; Valeev, V. A.; Glamazda, A. Y.; Plokhotnichenko, A. M.; Stepanian, S. G. Interaction of Fragmented Double-Stranded DNA with Carbon Nanotubes in Aqueous Solution. *Mol. Phys.* **2006**, *104*, 3193–3201.
- (42) Iliafar, S.; Mittal, J.; Vezenov, D.; Jagota, A. Interaction of Single-Stranded DNA with Curved Carbon Nanotube Is Much Stronger Than with Flat Graphite. *J. Am. Chem. Soc.* **2014**, *136*, 12947–12957.
- (43) Lu, G.; Maragakis, P.; Kaxiras, E. Carbon Nanotube Interaction with DNA. *Nano Lett.* **2005**, *5*, 897–900.
- (44) Meng, S.; Maragakis, P.; Papaloukas, C.; Kaxiras, E. DNA Nucleoside Interaction and Identification with Carbon Nanotubes. *Nano Lett.* **2007**, *7*, 45–50.
- (45) Staii, C.; Johnson, A. T.; et al. DNA-Decorated Carbon Nanotubes for Chemical Sensing. *Nano Lett.* **2005**, *5*, 1774–1778.
- (46) Paredes, J. I.; Villar-Rodil, S. Biomolecule-Assisted Exfoliation and Dispersion of Graphene and Other Two-Dimensional Materials: A Review of Recent Progress and Applications. *Nanoscale* **2016**, *8*, 15389–15413.
- (47) Zhang, G.; Zhang, X.; Yang, Y.; Zhang, H.; Shi, J.; Yao, X.; Zhang, X. Near-Infrared Light-Triggered Therapy to Combat Bacterial Biofilm Infections by MoSe<sub>2</sub>/TiO<sub>2</sub> Nanorod Arrays on Bone Implants. *Adv. Mater. Interfaces* **2020**, *7*, 1901706.
- (48) Gaur, A. P. S.; Sahoo, S.; Ahmadi, M.; Dash, S. P.; Guinel, M. J. F.; Katiyar, R. S. Surface Energy Engineering for Tunable Wettability through Controlled Synthesis of MoS2. *Nano Lett.* **2014**, *14*, 4314–4321.
- (49) Gurarslan, A.; Yu, Y.; Su, L.; Yu, Y.; Suarez, F.; Yao, S.; Zhu, Y.; Ozturk, M.; Zhang, Y.; Cao, L. Surface-Energy-Assisted Perfect Transfer of Centimeter-Scale Monolayer and Few-Layer MoS<sub>2</sub> Films onto Arbitrary Substrates. *ACS Nano* **2014**, *8*, 11522–11528.
- (50) Lei, Z.; Zhou, Y.; Wu, P. Simultaneous Exfoliation and Functionalization of MoSe<sub>2</sub> Nanosheets to Prepare "Smart" Nanocomposite Hydrogels with Tunable Dual Stimuli-Responsive Behavior. *Small* **2016**, *12*, 3112–3118.
- (51) Zheng, M.; Jagota, A.; Semke, E. D.; Diner, B. A.; Mclean, R. S.; Lustig, S. R.; Richardson, R. E.; Tassi, N. G. DNA-Assisted Dispersion and Separation of Carbon Nanotubes. *Nat. Mater.* **2003**, *2*, 338–342.
- (52) Backes, C.; Campi, D.; Szydlowska, B. M.; Synnatschke, K.; Ojala, E.; Rashvand, F.; Harvey, A.; Griffin, A.; Sofer, Z.; Marzari, N.; Coleman, J. N.; O'Regan, D. D. Equipartition of Energy Defines the Size—Thickness Relationship in Liquid-Exfoliated Nanosheets. *ACS Nano* 2019, *13*, 7050–7061.
- (53) Backes, C.; Szydłowska, B. M.; Harvey, A.; Yuan, S.; Vega-Mayoral, V.; Davies, B. R.; Zhao, P.-l.; Hanlon, D.; Santos, E. J. G.; Katsnelson, M. I.; Blau, W. J.; Gadermaier, C.; Coleman, J. N. Production of Highly Monolayer Enriched Dispersions of Liquid-Exfoliated Nanosheets by Liquid Cascade Centrifugation. ACS Nano 2016, 10, 1589–1601.
- (54) Liang, L.; Hu, W.; Xue, Z.; Shen, J.-W. Theoretical Study on the Interaction of Nucleotides on Two-Dimensional Atomically Thin Graphene and Molybdenum Disulfide. *FlatChem.* **2017**, *2*, 8–14.
- (55) Vovusha, H.; Sanyal, B. Adsorption of Nucleobases on 2D Transition-Metal Dichalcogenides and Graphene Sheet: A First Principles Density Functional Theory Study. *RSC Adv.* **2015**, 5, 67427–67434.
- (56) Phillips, J. C.; Braun, R.; Wang, W.; Gumbart, J.; Tajkhorshid, E.; Villa, E.; Chipot, C.; Skeel, R. D.; Kalé, L.; Schulten, K. Scalable

- Molecular Dynamics with NAMD. J. Comput. Chem. 2005, 26, 1781–1802.
- (57) Humphrey, W.; Dalke, A.; Schulten, K. VMD: Visual Molecular Dynamics. *J. Mol. Graphics* **1996**, *14*, 33–38.
- (58) Vanommeslaeghe, K.; Hatcher, E.; Acharya, C.; Kundu, S.; Zhong, S.; Shim, J.; Darian, E.; Guvench, O.; Lopes, P.; Vorobyov, I.; Mackerell, A. D., Jr. Charmm General Force Field: A Force Field For Drug-Like Molecules Compatible with the Charmm All-Atom Additive Biological Force Fields. *J. Comput. Chem.* **2010**, *31* (4), 671–690.
- (59) Hu, W. B.; Peng, C.; Luo, W. J.; Lv, M.; Li, X. M.; Li, D.; Huang, Q.; Fan, C. H. Graphene-Based Antibacterial Paper. *ACS Nano* **2010**, *4*, 4317–4323.
- (60) Mansukhani, N. D.; Guiney, L. M.; Kim, P. J.; Zhao, Y. C.; Alducin, D.; Ponce, A.; Larios, E.; Yacaman, M. J.; Hersam, M. C. High-Concentration Aqueous Dispersions of Nanoscale 2D Materials Using Nonionic, Biocompatible Block Copolymers. *Small* **2016**, *12*, 294–300.
- (61) Zhang, L.; Xu, B.; Wang, X. Cholesterol Extraction from Cell Membrane by Graphene Nanosheets: A Computational Study. *J. Phys. Chem. B* **2016**, *120*, 957–64.
- (62) Tu, Y.; Lv, M.; Xiu, P.; Huynh, T.; Zhang, M.; Castelli, M.; Liu, Z.; Huang, Q.; Fan, C.; Fang, H.; Zhou, R. Destructive Extraction of Phospholipids from Escherichia coli Membranes by Graphene Nanosheets. *Nat. Nanotechnol.* **2013**, *8*, 594–601.
- (63) Geoffrion, L. D.; Hesabizadeh, T.; Medina-Cruz, D.; Kusper, M.; Taylor, P.; Vernet-Crua, A.; Chen, J.; Ajo, A.; Webster, T. J.; Guisbiers, G. Naked Selenium Nanoparticles for Antibacterial and Anticancer Treatments. ACS Omega 2020, 5, 2660–2669.
- (64) Vahdati, M.; Tohidi Moghadam, T. Synthesis and Characterization of Selenium Nanoparticles-Lysozyme Nanohybrid System with Synergistic Antibacterial Properties. *Sci. Rep.* **2020**, *10*, 510.
- (65) Mei, L.; Zhu, S.; Yin, W.; Chen, C.; Nie, G.; Gu, Z.; Zhao, Y. Two-Dimensional Nanomaterials Beyond Graphene for Antibacterial Applications: Current Progress and Future Perspectives. *Theranostics* **2020**, *10*, 757–781.
- (66) Nečas, D.; Klapetek, P. Gwyddion: An Open-Source Software for SPM Data Analysis. Cent. Eur. J. Phys. 2012, 10, 181–188.

# NOTE ADDED AFTER ASAP PUBLICATION

This paper was published on the Web on February 11, 2021, with *Eschericia coli* and *Staphylococcus aureus* identified as Gram-negative instead of Gram-positive in the Abstract. The corrected version was reposted on February 16, 2021.